Development of a 3D-printed phantom for proton therapy

Rogier van Oossanen

Supervised by: dr. Eelco Lens

Master thesis performed at:

Medical Physics & Technology

Department Radiation, Science and Technology

Facility of Applied Sciences

Delft University of Technology

REACTOR INSTITUTE DELFT

To be examined by:

Dr. Ir. D.R. Schaart

Prof. Dr. C.C.L. Wang

Dr. Z. Perko

Abstract

Proton therapy is a relatively new technique in the field of radiation oncology. The advantage of using protons can be illustrated by the depth-dose relation, which results in a more concentrated dose at a specific depth and thus potentially less dose in the surrounding healthy tissue compared to conventional photon therapy. However, this depth-dose relation also makes the dose delivery very sensitive to small geometric uncertainties. Because of this sensitivity, high accuracy of the quality assurance (QA) is essential.

QA can be used to test robustness of the system when dealing with small geometric uncertainties such as air gaps. Most of the QA protocols use phantoms to test the clinical treatment protocol or the complete treatment chain. To accurately simulate a patient, the phantom should resemble the human anatomy as well as tissue composition its interaction properties with ionizing radiation. In order to be optimally test the accuracy of the treatment system, the phantom should include small air gaps, density gradients in soft and bone tissue-substitutes and millimeter-scale structures. Currently phantoms are produced using casting techniques, which limits the possibilities to include small features or density gradients. This causes the phantoms available to lack the level of detail required for proton therapy QA.

One important source of errors in current treatment planning is the usage of a mono energy CT-scan of the patient for treatment planning, which measures the photon attenuation and converts this to Hounsfield Units (HU). For proton therapy, the HU is converted to the proton stopping power ratio (SPR) of the tissue compared to water, using a HU-SPR conversion model. Since there is no one-to-one relation between HU and SPR, this inevitably leads to errors, for example when tissues with the same HU have a slightly different SPR. Therefore dual-energy CT (DECT) has been proposed as a replacement for conventional mono energetic CT in proton treatment planning. The information acquired by the DECT is used in the Bethe formula to calculate the SPR directly, making the HU-SPR calibration curve obsolete, thus improving the accuracy of treatment planning.

The goal of this study is to explore the possibilities of designing an anthropomorphic phantom with small geometric features using a 3D-printer. By using a 3D-printer we can print the structure of the phantom at the millimeter-scale. Multiple materials can be mixed while printing, making it easier to adjust material properties such as density. Since DECT could improve proton treatment planning, we will aim to use materials that will be compatible with DECT-based HU-SPR conversion methods, so that these materials will be treated similar to that of human tissue by the treatment system. This way, the phantom should have the same SPR as human tissue, as well as covering small geometric details.

Contents

Introduction

Proton therapy is a relatively new technique in radiotherapy, where protons instead of photons are used to irradiate tumours. Although the advantages of proton therapy were already discussed in 1946 [1], the first proton therapy centre opened in 1990 [2]. Proton therapy treatment systems have been commercially available since 2001, and since then the availability of proton therapy has increased rapidly [3].

The main advantage of proton therapy over photon therapy is related to the dose-depth profile of protons, which is shown in Figure 1. With proton therapy the dose in the tumour is accumulated using multiple proton beams with different energies to create a uniform dose distribution within the tumour, called a spread-out Bragg peak. The dose depth curve of a single beam with one energy is strongly peaked at a specific depth (i.e. the Bragg peak) that is dependent on the initial proton energy [4]. Compared to photons the dose delivered by protons before the tumour is lower, and behind the tumour is zero.
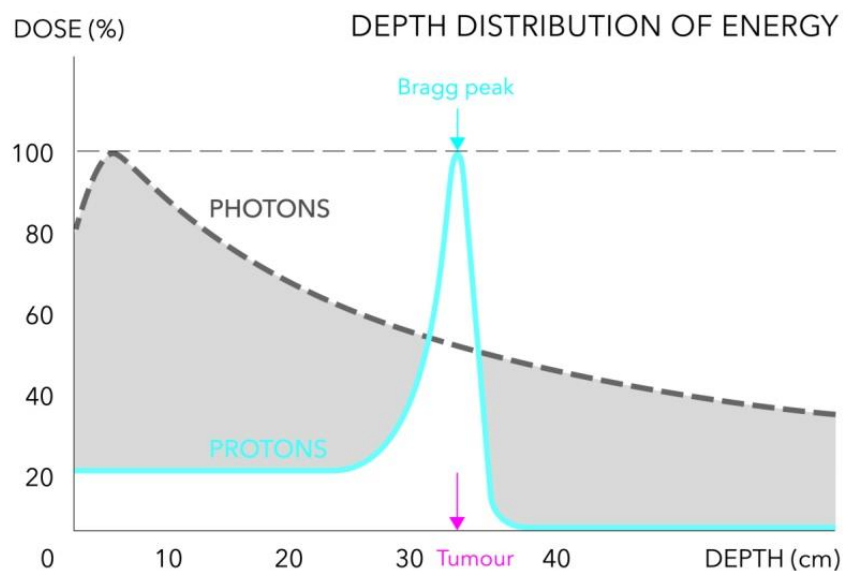

Figure 1 Dose depth distribution of photons (in grey) and protons (in blue), with dose normalized to the dose in the tumour. [5]

The sharp dose fall-off after the spread-out Bragg peak is an advantage of proton therapy, as it could be used to reduce the dose to organs at risk behind the tumour. This makes proton therapy very suitable for treating tumours close to critical organs [6]. However, it also introduces additional uncertainties, as a slight shift of the dose distribution can now reduce the dose in part of the tumour to almost zero, while with photon therapy a similar shift would result in only a slightly different dose in the tumour.

There are many sources of uncertainty in proton therapy. This research is focused on only two sources of uncertainty that are relevant for the design of a phantom. The first one is the uncertainty

introduced by the heterogeneous nature of human tissue. As the range of protons is determined by the type of material in the beam path, it is sensitive to changes in the anatomy of the patient. Compared to photon therapy, proton therapy is much more sensitive to small geometric uncertainties that come with heterogeneous tissues. The other source of uncertainty is conversion of photon attenuation measured with a CT scanner to proton stopping power that is needed to calculate a treatment plan.

In proton therapy QA, these uncertainties are tested, quantified and minimized. To test the TPS for these uncertainties, an anthropomorphic phantom is used to simulate a clinical patient. To test for uncertainties caused by heterogeneities in human tissue, the phantoms could include small air gaps, bone fractions, density gradients in both soft and bone tissue or a liquid-filled bladder-substitute. In order to test the quality of the photon attenuation to proton stopping power conversion, the phantom should be composed of materials that behave similarly in terms of photon and proton interaction to human tissues. The exact requirements rely on the conversion method used.

This study aims to explore the possibilities of designing a new phantom for QA in proton therapy. This is necessary since currently commercially available phantoms do not meet the requirements: accurately simulating small geometric details that are present in patients, and secondly, interact similar to human tissue with photons and protons. The latter is needed to accurately simulate the conversion from photon attenuation to proton stopping power in the treatment planning system (TPS) in a clinical patient. To achieve this, we focus on additive manufacturing, also known as 3D printing. An impression of the level of detail that can be acquired with additive manufacturing is shown in Figure 2.

Ultimately, we strive to develop a phantom can accurately simulate a clinical patient during the whole treatment cycle. Starting with an initial planning-CT, after which the TPS calculates a treatment plan, the treatment plan is delivered. With a correctly calibrated TPS, the dose distribution in the phantom should be the same as the treatment plan calculated, and thus as it would be in a clinical patient.
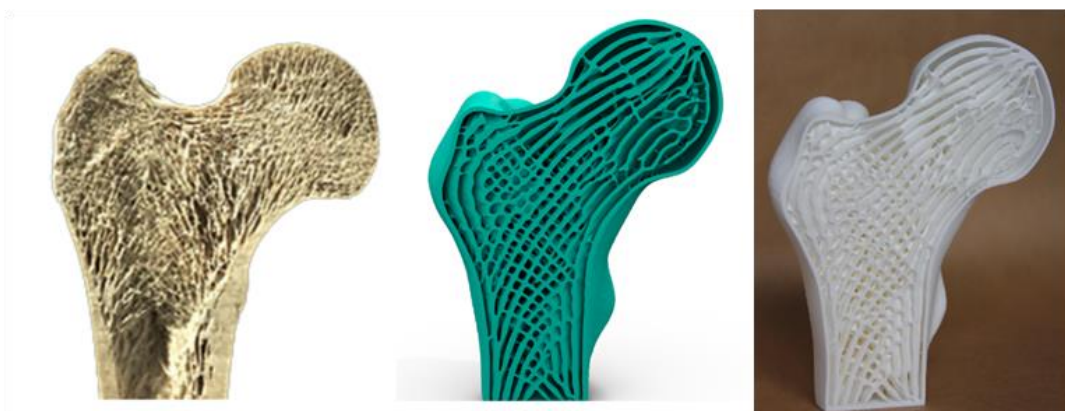

Figure 2. An example of the level of detail that can be acquired with 3D-printing. On the left a cross-section of a human hip bone is shown, in the middle an image of a 3D-model made with the computer, and on the right a photograph of the 3D-printed model. Pictures from Jun Wu et al [7].

Theory

Phantoms

Phantoms have played a major role in the medical world for the last century as a substitute for humans in ionizing radiation applications. In QA of CT- and radiotherapy systems phantoms are used as the main testing object, while they are also used for developing and testing of new imaging modalities and treatment methods. Although one of the first phantoms ever used, a water container with a dosimeter inside [8], is still widely used nowadays, anthropomorphic phantoms have become more popular.

For a phantom to be tissue-equivalent, the materials that the phantom is composed of should ideally interact with radiation in the same way as human tissue. As this behaviour depends on the type of radiation used, i.e. high- or low-energy photons, beta-particles or protons, the materials that behave tissue-equivalent also change. Many materials have been used to mimic human tissue for radiation purposes, however the current production techniques make detailed phantoms expensive and untailored to specific needs [9]. To increase the level of detail and enable the manufacturing of patient-specific phantoms, 3D printing techniques can be used.

The history of phantoms starts with the research on tissue-equivalent materials. The first research on this topic goes back to 1906, where Kienböck stated that 'an aluminium foil 1 mm thick is equivalent in absorption power to a layer of water or muscle, 1 cm thick' [10], which was the first statement on tissue-equivalence of a material. Franz Christén expanded the field with the publication of his book 'Messung und Dosierung der Roentgenstrahlen' in 1913 [11]. He was the first to state that water should be used both as a soft tissue equivalent and water attenuation as a parameter for x-ray beams. In 1922 Baumeister proposed wax as a soft-tissue equivalent [12]. After this initial research, the field of dosimetry expanded and most researchers used either water of wax as a tissue-substitute [13]. In fact, water is still used as a standard in radiology and radiotherapy [14]. The first anthropomorphic phantoms in the shape of (part of) the human body is described in 1924 [15]. Since the clinical use of ionising radiation showed a rapid growth, so did the research and production of phantoms [8], [16]–[18].

Current commercially available phantoms are almost exclusively made using casting techniques, and the level of detail stretches from barely recognizable as humans to phantoms that contain parts of actual human skeletons. With a rising level of details also comes a rising level of costs. An overview of currently available phantoms was given by DeWerd [14].

An example of a modern anthropomorphic phantom are the IMRT phantoms of the Radiological Physics Center (RPC). In Figure 3a, the head and neck, pelvis and lung phantoms are shown, as well as CT slices of the phantom compared to an actual patient (3b and 3c). The phantoms have been described in literature, and are still used for QA [19]–[21]. As can be seen from the figure, the level of detail is poor and insufficient for state of the art QA of proton therapy.
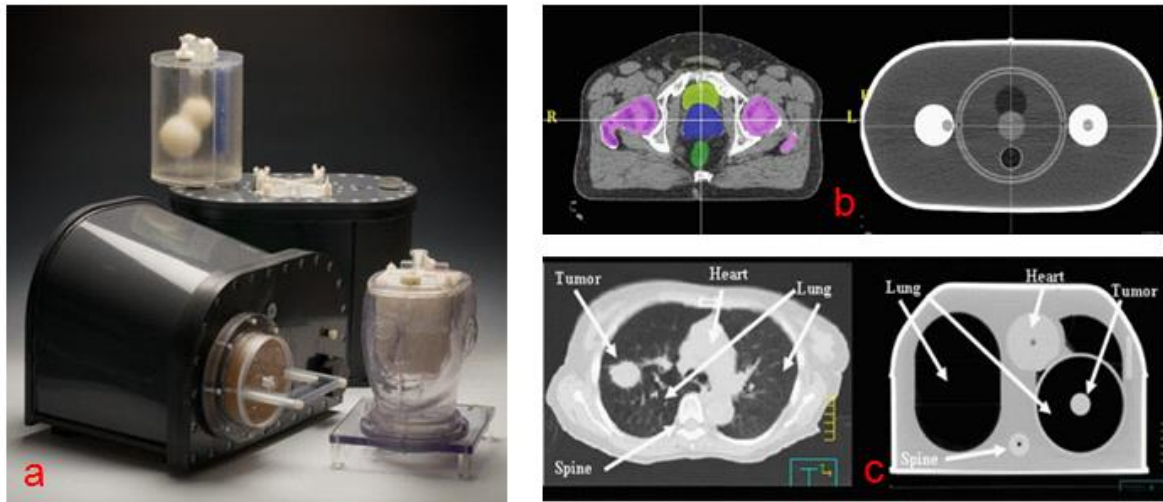
Figure 3. The RPC IMRT Head and neck, pelvis and lung phantoms. a) A photograph of the phantoms. b) On the left a CT image of the pelvis of a prostate patient, on the right a CT image of the pelvic phantom. c) On the left a CT image of the lungs of a lung cancer patient, on the right a CT image of the lung phantom.

Figure 4a shows an anthropomorphic head phantom. This is the commercially available CIRS head-phantom [22]. This phantom has been used in a recent study by Farace [23]. This phantom shows a greater level of detail than the RPC IMRT phantoms. However, the small air gaps that can be seen in Figure 4c, are not represented in the phantom (Figure 4b) while these small gaps are a perfect example of small geometric uncertainties that can potentially affect the delivered proton dose. Also, we can see that there is a gradient in HU, and thus proton stopping power, in the human bone is large while in the phantom there are only two bone materials, one with a higher and one with a lower HU.
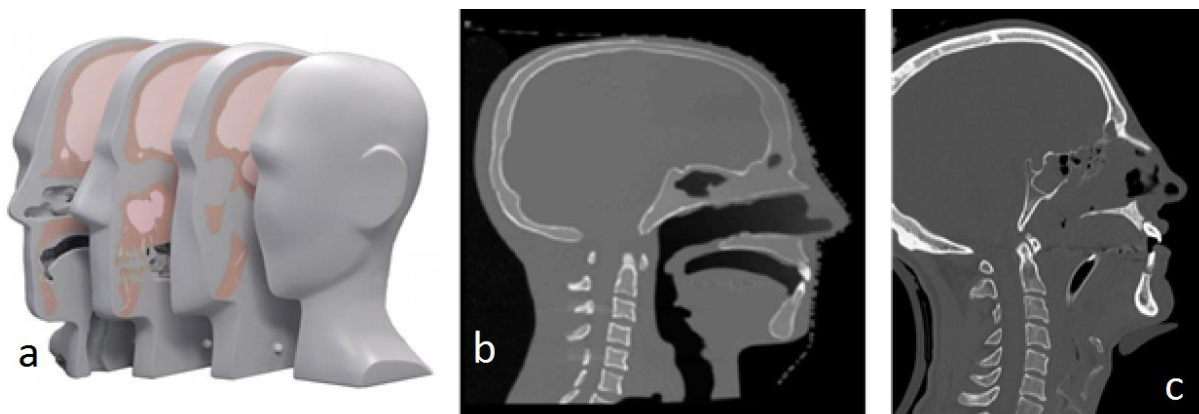
Figure 4. The CIRS Proton Therapy Head Phantom 731-HN. a) A photograph of slices of the phantom. b) A CT image of the phantom c) A CT image of an actual patient [22], [23]**.**

Although these are just three examples of the available phantoms, it shows that these phantoms lack the level of detail on the millimeter scale. QA in proton therapy aims at an accuracy of dose delivery within a few millimeter [24]. To perform proper proton therapy QA, a phantom should be available which accurately presents the inhomogeneous nature of the human body.

Photon attenuation

For proton therapy treatment planning, the photon attenuation is used to determine the proton stopping power. This is not trivial, as the photon attenuation and proton stopping power of a material are caused by different ways of interaction of the photons and protons with the material they are passing through. The attenuation of photons with an energy around 100 keV, the energy of the photons typically used in a CT scanner, is caused by two mechanisms that act independently and both contribute to the total attenuation.

The first mechanism is the photo-electric effect, where the photon hits an electron bound in a shell of an atom. The electron absorbs all the energy of the photon, which brings the electron to an excited state or even causes it to become a free electron (when the photon energy is greater than the binding energy). This leaves a gap in the electron shell and when this gap is filled by another electron from an outer shell, a new photon is emitted with the difference in binding energy between the outer shell and the new position in the inner shell. The energy of this newly emitted photon is always lower than the energy of the original photon.

For the photoelectric effect, the chance of interaction between the photon and electron is higher with electrons with a higher binding energy, i.e. the inner electrons. As the binding energy increases when the atomic mass increases, the chances of the photoelectric effect happening increases with increasing atomic number (Z). The interaction probability is also dependent on the energy of the photon. The photoelectric absorption can be written as [25]

$$\mu = \rho_e \frac{Z^n}{E^3} \tag{1.1}$$

Where ρ_e stands for the electron density, Z is the effective atomic number and E the energy of the photon. It is reported that n should be around 3 for human tissue [25].

The second mechanism is the Compton effect (e.g. Compton scattering), this is also caused by an interaction between the photon and an electron. However, this effect mostly occurs with the outer, less bound electrons. With Compton scattering the photon hits the electron and part of the energy of the photon is transferred to the electron. A new photon is created with an energy lower than the initial photon energy. This photon will continue with a lower energy and may have a different direction than the original photon. Furthermore, the electron becomes a free electron with a kinetic energy equal to the energy received from the photon minus the binding energy. The probability of Compton scattering is dependent on the electron density, the more electrons the higher the chance of interaction, and the energy of the photon. The Compton scattering cross-section can be written as:

$$\mu = \rho_e f(E) \tag{1.2}$$

Where ρ_e is the electron density and $f(E)$ is a function dependent on the energy of the photon, which is almost constant for the photon energy used in a CT-scanner [26]. The total attenuation is the sum of the attenuation due to the photoelectric effect and the Compton effect (1.3).

$$\mu_{total} = \mu_{photo} + \mu_{compton} = \rho_e \frac{Z^n}{E^3} + \rho_e f(E) \tag{1.3}$$

The ratio between the attenuation due to photoelectric effect and Compton effect changes depending on the x-ray spectrum. The formula shows that the photon attenuation of a material at a given energy depends on the effective Z and the electron density of the material.

Proton interactions

While photons are uncharged particles without mass, protons have both charge and mass. Therefore, they interact in a different way than photons when travelling through a material. Photons either interact with the material, which will make the photon disappear and might create a new photon, or they pass through the material without interaction. Protons however have a lot of smaller interactions with the material, causing them to gradually lose kinetic energy and slow down.

There are three types of interaction protons can have with the material they are travelling through. These interactions are called stopping, scattering and nuclear interactions. Almost all interactions are either stopping or scattering, however sometimes the proton has a inelastic interaction with a nucleus. This results in one or more secondary particles being send out of the nucleus, which can be gammas, protons, neutrons or even small complexes of protons and neutrons, such as a helium nucleus [27]. Although these heavy ions have a large relative biological effect (RBE), and in theory can give rise to a large local dose, research has shown that the effect of these nuclear interactions on the total dose distribution is rather small [28], [29]. This is caused by the low amount of energy that is transferred into these heavy ions. Most of the energy ends up in protons, neutrons and photons [29]. Thus for a phantom for proton therapy, heavy-ion interactions are not significant for tissue-equivalence.

The mechanisms of stopping and scattering are caused by electromagnetic interactions between the positively charged proton and the charges of either the atomic electrons or the nucleus. Scattering of the proton can happen when the proton is deflected by the positive charge of the nucleus, however the angle of deflection is extremely small at proton therapy energies (around 200MeV). Although many of these small deflections together cause the proton beam to spread a little, this is a minor effect that is well understood [30], [31]. The angle of the scattering increases rapidly when Z increases [32].

The main part of the behaviour of protons passing through a material can be described by the stopping mechanism. Protons constantly interact with atomic electrons, transferring kinetic energy to the electron and decreasing its own velocity. The energy transferred to the electron increases when the kinetic energy of the proton decreases. This can be explained by the proton and the electron having a larger timeframe to interact with each other when the velocity of the proton is smaller, thus a larger energy transfer [33]. This effect is reflected in the shape of the Bragg peak.

Bethe-Bloch formula

The range of protons is largely determined by the stopping mechanism, which can be described with the proton stopping power. The proton stopping power is defined as the amount of kinetic energy that is lost per unit of length in the material:

$$S \equiv -\frac{dE}{dx}.$$

(1.4)

Where S is the proton stopping power, E the kinetic energy of the proton and x the distance travelled through the material. The interaction between charged particles and atomic electrons has been studied extensively and already in 1933 Bethe and Bloch derived the formula for the energy lost by a charged particle travelling through a material [34]. The original formula for relativistic stopping power is:

$$S = \frac{4\pi e^4 Z_2}{m_c v^2} Z_1^2 \left[\ln \frac{2mv^2}{I} - \ln\left(1 - \beta^2\right) - \beta^2 + \Psi\left(Z_1\right) \right].$$ (1.5)

Where I is the mean excitation potential per electron, e the electron charge, Z_1 and Z_2 the effective Z of the travelling ion and the material, respectively, m_e the electron mass and β the relative particle velocity, v/c. The last term, Ψ is a correction added by Bloch. For protons, this can be rewritten as:

$$S = \frac{4\pi \rho_e}{m_e c^2 \beta^2} \cdot \left(\frac{e^2}{4\pi\varepsilon_0}\right)^2 \cdot \left[\ln\left(\frac{2m_e c^2 \beta^2}{I \cdot \left(1 - \beta^2\right)}\right) - \beta^2 \right].$$ (1.6)

Since most of these terms are constant, we get:

$$S = K_1 \frac{\rho_e}{\beta^2} \cdot \left[\ln\left(K_2 \cdot \frac{\beta^2}{1 - \beta^2} \cdot \frac{1}{I} \right) - \beta^2 \right].$$ (1.7)

Which shows that the proton stopping power of a material is dependent on electron density and mean ionization potential.

Treatment planning in proton therapy

Radiation treatment planning starts with making a CT-scan of the patient. During a CT-scan, low-energy (typically in the range of $80 - 140$ kEv) x-ray radiation is send through the body from different angles. Depending on the tissue types that the x-ray travels through, the attenuation of the x-ray varies. By measuring the x-ray attenuation through the body from multiple angles, a 3D-reconstruction can be made of the attenuation of the body. In CT-scans, the attenuation is expressed in Hounsfield Units (HU), which is the x-ray attenuation relative to the attenuation of water. Formula (1.8) shows the formula to calculate the HU, with μ being the attenuation coefficient given by:

$$HU = 1000 \cdot \frac{\mu - \mu_{water}}{\mu_{water} - \mu_{air}}.$$ (1.8)

The acquired CT-scan shows the anatomy of the patient, as different tissue types have different HU. This is used by the physician to delineate the tumour site in the CT-scan, which determines the planning target volume. The planning target volume is the area in the patient that should get irradiated and includes the tumour with some safety margins around it. Then this information is send to the TPS which will use this information to calculate a treatment plan based on clinical objectives and constraints. During treatment planning, the TPS determines the proton stopping power in the patient based on HU. Basically, the photon attenuation is converted to proton stopping power.

In medical practice proton stopping powers are expressed in pathway relative to water, since most calibrations are still performed using a pool of water and an ionisation chamber. Instead of proton stopping power, the stopping-power ratio (SPR) is used. This is simply the stopping power of the material divided by the stopping power of water.

Proton stopping power determination

To determine the proton stopping power using CT-images, Schneider et al. [35] performed a calibration of CT Hounsfield Units to SPR in 1995, using both tissue-substitutes and real tissue from a sheep's head. They proposed a stoichiometric calibration. The stoichiometric calibration was needed as the HU of human tissue slightly changes for different CT-systems. Ideally, all these systems would be calibrated using real human tissue, however this is practically impossible. To be able to perform the calibration using tissue-substitutes, the stoichiometric calibration uses the measured HU of tissue-substitutes together with the chemical composition of real tissues to predict HU for human tissues, which is then used in combination with measured proton stopping power of human tissue to make a one-to-one mapping of HU to SPR. The resulting fit is shown in Figure 5 and Figure 6.
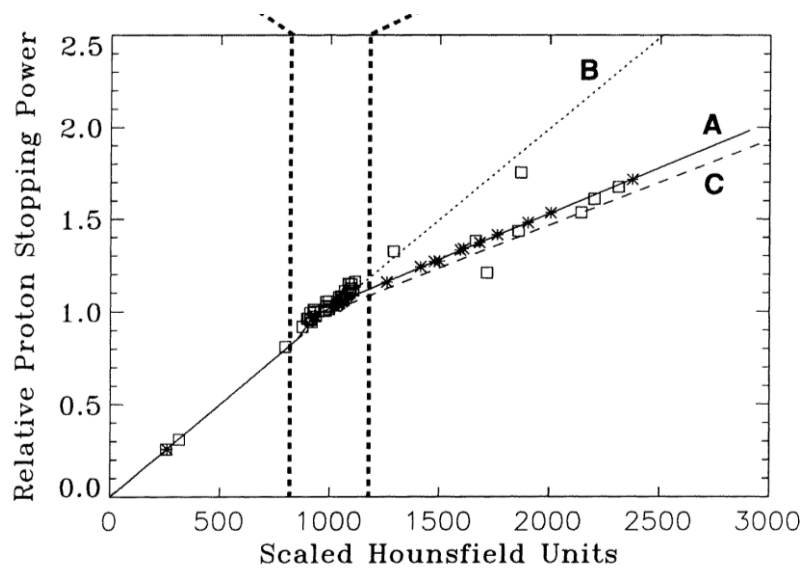

Figure 5. Graph of Hounsfield Units versus SPR, the conventional calibration curve as proposed by Schneider et al. The squares represent phantom materials while the crosses represent human tissues. The solid line is the stoichiometric calibration curve for biological tissue, the dotted and dashed lines are tissue substitute calibrations. A zoom-in of the area delineated with the dotted line can be found in Figure 6 [35].

Currently, most proton therapy TPS determine the proton stopping power using a HU-SPR conversion as published by Schneider et al. The formula's (1.3) and (1.7) show that photon attenuation depends on electron density and effective atom number when the energy of the photons is kept constant, while proton stopping power depends on electron density and mean ionization potential. Because the effective atom number and the mean ionization potential are not one-on-one related, there is also not a one-on-one relationship between photon attenuation and proton stopping power. However, Pedroni showed in 1998 that when determining the SPR of human tissue, this does not lead to great errors [36]. The conversion is accurate because there is extra information when determining the SPR, namely that the material is human tissue. There is only a limited number of different tissue types in the sense of both proton stopping power and photon attenuation. Because

the tissue types had unique photon attenuation, these could be differentiated based on the HU and thus assigned their unique SPR.

Unfortunately it turned out to be not as accurate as was thought. Recently there have been reports that accuracy of the SPR determination is lacking as sometimes tissues with the same HU may have different SPRs [26], [37]. Comparing treatment plans calculated with the HU-SPR conversion method to Monte Carlo simulations showed additional errors [38]. Additionally metallic implants can cause artefacts in the CT scan, and as these are not included in the calibration the SPR assigned to these metallic implants is incorrect. This can decrease the accuracy of the treatment plan [39], [40]. In addition, the research of Schneider et al. showed that current tissue-substitute materials are not tissue-equivalent for proton therapy. As can be seen in Figure 5 and Figure 6, most phantom materials don't fit the calibration line proposed by Schneider et al.
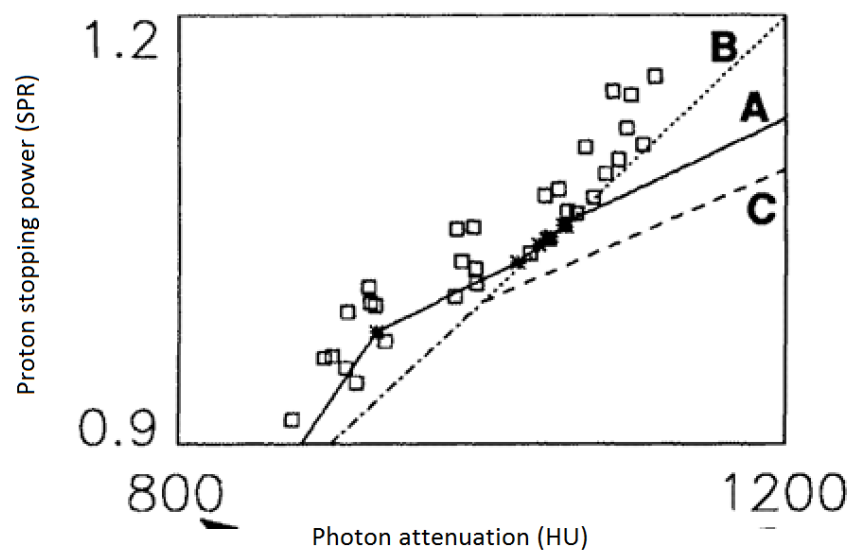

Figure 6. Close-up of the HU-SPR calibration curve proposed by Schneider et al. On the x-axis the photon attenuation is given in HU, on the y-axis the SPR is given (without unit). The squares represent phantom materials, the crosses are human tissue. The solid line is the stoichiometric calibration curve for biological tissue, the dotted and dashed lines are tissue substitute calibrations [35]**.**

This introduced difficulties in proton therapy QA because if one wants to test the whole process from planning CT to dose delivery, a phantom is required that fits on this calibration curve. If this is not true, the TPS will assign a wrong SPR to the phantom material, resulting in a faulty treatment plan. This was also reported by Grant et al. on behalf of the Radiological Physics Center, who investigated the suitability of different phantom materials for the use in proton therapy phantoms [41].

Grant et al. showed that commonly used tissue-substitute materials could have a large difference between the SPR assigned by the TPS and the actual SPR. Examples are PMMA (10.3% difference), Nylon (12.2%) and bone meal (31.5%). Some materials are more suited, such as polyethylene (1.9%) and CIRS Bone (4%). Since the HU/SPR calibration depends on the CT-scanner and TPS used the results will be different for different systems.

In an attempt to increase the accuracy of proton range determination, scientist have looked for other methods. Using protons to image the patient gives you direct information about the proton stopping power. A lot of research has been done recently on this new technique, proton CT [42]–[45].

However it is still in an early research state and not yet clinically available. Other techniques used to gain more information on the tissue include dual energy CT, PET-MRI, PET-CT, MRI and optical coherence tomography [26]. Dual energy CT is the technique that we will investigate further, as this is already clinically available in modern proton therapy centres such as HollandPTC, where we collaborated with.

Dual energy CT

Dual energy CT (DECT) is a relatively new technique, with its first evaluation published in 2006 [46]. However the idea of using two photon spectra with different mean energies to determine effective atomic mass number and electron density was already performed in 1976 by Rutherford [47]. After its first use the dual energy CT has been studied extensively, and it has been shown that DECT can be used to determine the electron density and effective atomic number [48]–[50].

From formula (1.3), it is clear to see that when calibrated for $f(E)$ and for the ratio between the photoelectric attenuation and the Compton attenuation, there are only two unknown parameters left for a given energy, namely the electron density and the effective Z. When measuring the same material twice at two different energies, the electron density and effective Z can be calculated. Recent studies showed that this can then be used to determine the proton stopping power.

In 2010 Yang published a method to measure the SPR of humans using dual energy CT [51]. The DECT can be used to determine electron density and effective atom number, while for SPR calculation using the Bethe formula electron density and ionization potential is needed. Yang therefore uses the effective atom number to look up the ionization potential from a reference table, which contains pre-calculated effective atomic numbers and corresponding ionization potentials for reference human body tissues. This method was experimentally validated by Hünemohr, who showed that the SPR could be determined with an accuracy of 0.6% for homogeneous phantoms of tissue equivalent materials [26]. This approach does not work with mixtures of different materials since these are not included in these reference tables. The tabulated values show a gap of data between soft tissue and bone tissue. In practice however often a CT-voxel is filled with both parts of bone tissue and soft tissue, so the HU is somewhere in between soft and bone tissue. The gap in tabulated values between soft tissue and bone makes it impossible to assign SPRs to CT voxels that contain such mixture of bone and soft tissue. This makes this approach currently still unsuitable for clinical practice. Therefore, Möhler proposed a new method to determine the SPR based on DECT, without using a reference table [52]. Möhler rewrites the equation for photon attenuation, (1.3):

$$\mu = \rho_e \sigma. \tag{1.9}$$

Where σ is the photon absorption cross section per electron, which is a function of the energy spectrum of the CT scanner and the effective Z of the material. In a mixture, the total attenuation coefficient is the sum of the attenuation coefficients of the different compounds in the material. Here the photon attenuation is expressed in the two variables ρ_e and σ. The σ contains the same
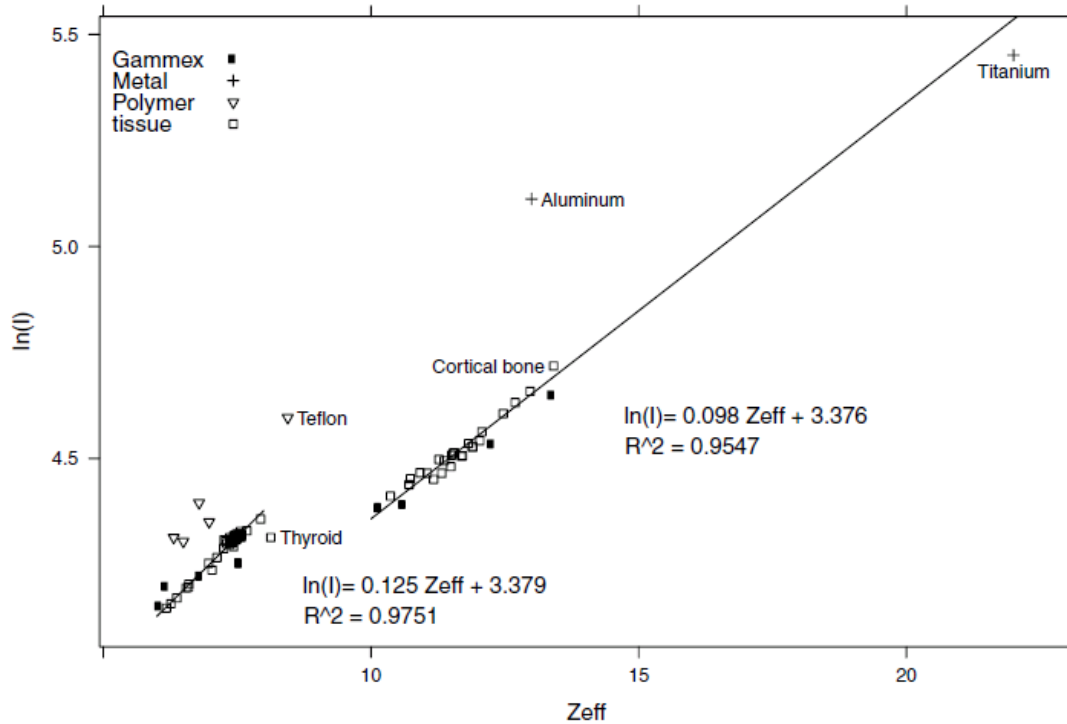
Figure 7. ln(I), the ionization potential, versus the effective atom number Zeff, fit of 71 tabulated tissues, Gammex surrogates, polymers and two measured metals by Hünemohr. The low left side resembles soft tissue, the middle part the bone tissue [26]**.**

information as the effective Z, but is more straight-forward to determine and doesn't require the assumptions that are made when determining the effective Z using DECT [52].

Using the Bethe formula, Möhler writes the SPR as:

$$\hat{S} = \hat{\rho}_e \frac{L(I,\beta)}{L(I_w,\beta)} =: \hat{\rho}_e \hat{L}.$$

(1.10)

Where the SPR is a product of the mean electron density and a function L of the ionization potential and the energy of the proton, expressed as the speed relative to the speed of light, β. The ^ above a variable shows that it is relative to water, for example $\hat{\rho}_e = \rho_e / \rho_{e,water}$. The $\hat{L}$ is called the relative stopping number. Möhler reported that the variation in SPR is caused for about 95% by the electron density, which can be directly measured using DECT, and 5% by the ionisation potential L [52].

Möhler neglects the shell, density and Bloch corrections in the Bethe formula, which is allowed for protons of therapy energy around 200MeV. These corrections are only significant for lower energies in the order of a few MeV of less. Without these corrections, L can be expressed as:

$$L(I,\beta) = \ln \frac{2m_e c^2 \beta^2}{1-\beta^2} - \beta^2 - \ln I.$$

(1.11)

L depends logarithmically on the ionization potential I, which in practice causes L to be not very sensitive to small changes in I. The ionization potential can be looked up for both single elements and for elements as part of a composite material in work from Seltzer and Berger [53]. The changes in I

are limited within human tissue, from 63 eV in adipose tissue to about 112 eV in cortical bone. Möhler calculated that for this interval of I, the change in L is only a few percent, changing between a factor of 0.95-1.02 difference for therapy energy protons. See also Figure 8. Thus the ionization potential is a small factor in determining the SPR of human tissue, and an approximation using lookup tables is sufficient to determine L.
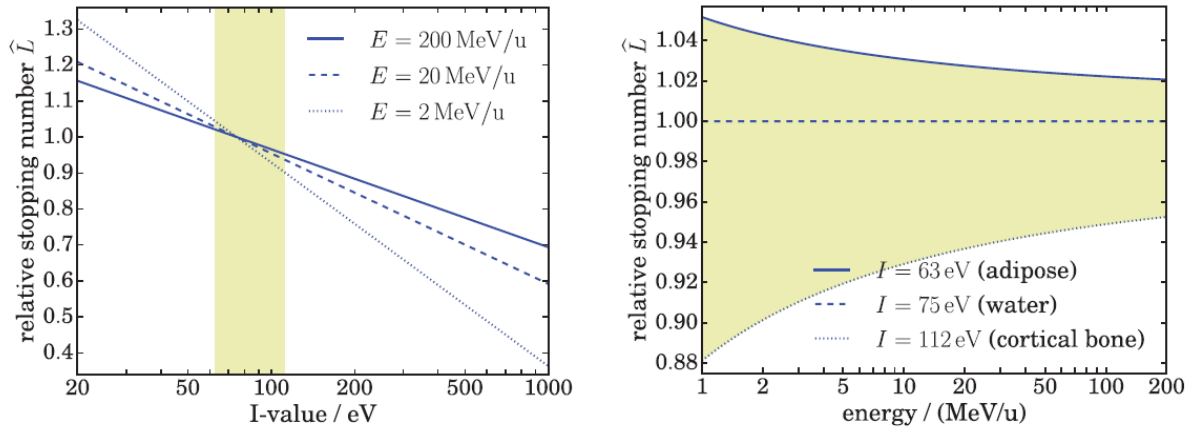

Figure 8. On the left the relative stopping number L is plotted versus the ionization potential I, for 3 different proton energies. On the right side the relative stopping number is shown versus the energy of the protons, for three ionization potentials. The gray areas mark the range of ionization potentials present in human tissue. Figure from Möhler [52].

Conform the additivity rule for stopping powers from Bragg [54], the total stopping power is simply the sum of the stopping powers of the individual compounds that make up the mixture. This can be extended to both σ and L:

$$S = \sum_i S_i \quad \sigma = \sum_i \sigma_i \quad L = \sum_i v_i L_i \tag{1.12}$$

Where v_i is the electron density fraction of the compound i, as a ratio to the total electron density. This makes it possible to express a mixture of compounds with an unknown (σ, L), as the sum of the (σ, L) of the compounds:

$$(\sigma, L)_{mixture} = \sum_i v_i (\sigma, L)_i \tag{1.13}$$

Using this, a (σ, L) map can be created by calibration that maps all σ to the corresponding L, so that the SPR can be calculated. This way the (σ, L) of all human tissue can be described as a linear combination of the (σ, L) of bone and soft tissue within about 1% [52].

Tissue-equivalence using two printing materials

Using the theory of Möhler, the (σ, L) property of human tissue can be simulated using two materials that in a linear combination add up to the (σ, L) of human tissue. This enables a new method of making tissue-equivalent phantom material. The (σ, L)-space of human tissue was

determined by Möhler and is shown in Figure 9. The brown area shows the space spanned by human tissues. As can be seen, the human tissue types can be approximated with a linear fit in the (σ, L) space, depicted with a brown dashed line, with a maximum deviation of about 2% from the outside of the human tissue space. Ideally, one could represent all human tissue types in the (σ, L) space with a linear combination of two ideal materials that lie on either side of the fitted brown dashed line. If these two materials were used to build a phantom, this phantom could represent all human tissue types within 2% accuracy. In reality, two such materials do not (yet) exist. However any two materials that in a linear combination cross the human tissue space, can represent part of the human tissues.

Note that, in theory, if three materials are used, a (σ, L) space can be spanned using a linear combination of these three materials. If this space includes the human tissue (σ, L) space, any point in the human tissue space could be represented by these three materials. This research was limited to the linear combination of only two materials.
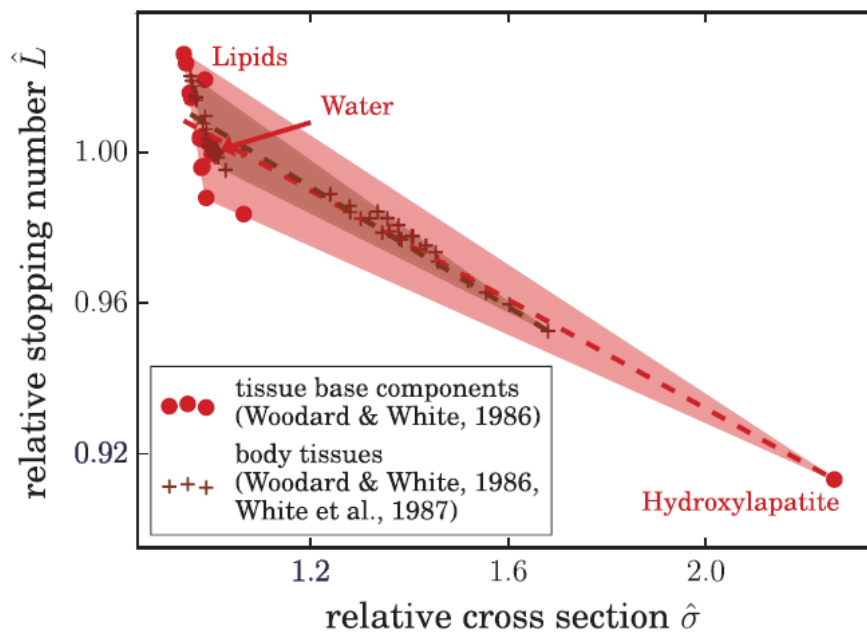

Figure 9. The (σ, L) space of human tissue and tissue base components, taken from Möhler [52]. **The brown triangle represents the** (σ, L) **space of human tissues. This space can be approximated by the brown dashed line. If two materials are used that are on either side of this brown line, any point in between can be made with a linear combination of these two materials.**

Materials and methods

Ultimaker 3

The 3D-printer that was used for the experiments is the Ultimaker 3, a fused deposition modelling printer. A schematic overview of the printer is shown in Figure 10. The print is made using a filament with a diameter 2.85 mm in diameter. The filament is led through a feeding motor, which can push the filament back and forth towards the heated extrusion nozzle, where it melts. The x and y direction form the plane parallel to the glass plate (Figure 10e), while the z direction is orthogonal to the glass plate. The nozzle can move in x and y direction, over a glass plate, on which the nozzle lays a string of the printing material. By laying the strings in a grid next to each other, the 3D-print is made layer by layer. After each layer, the glass plate moves one layer thickness down in the z direction. The smallest string the Ultimaker can print is 400 μm wide and has a thickness of 20 μm.
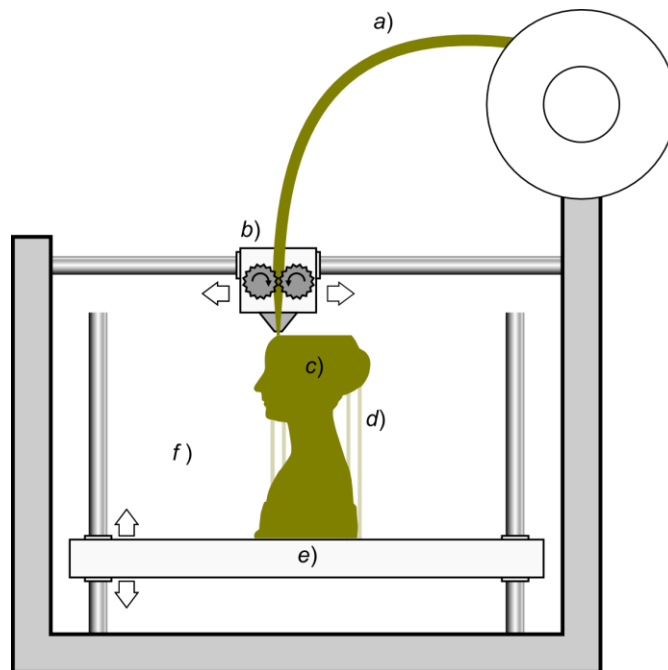

Figure 10. Schematic overview of a fused deposition modelling type printer. On the top right is the coil that contains the plastic filament (a). The filament is then led through a moving extrusion nozzle (b), which is heated to melt the plastic. The nozzle lays down a string of plastic on the 3D-print (c), of which the first layer is placed on a glass plate (e) [55]**.**

Fused deposition modelling printing has the advantage that two materials can be printed together in one print. However, it also has some shortcomings. First of all the printing technique is not tailored to be print large solid models. Most of the 3D-printed objects are hollow, with a density of about 20% to strengthen the print.

Another shortcoming is the limited types of material that can be printed. The materials that are commercially available for the Ultimaker 3 include polylactic acid (PLA), polyvinyl alcohol (PVA), Nylon, polyethylene terephthalate (PET) and acrylonitrile butadiene styrene (ABS), with and without additives. Our first experiment was based on these materials.

HU-SPR of printing materials

In order to determine the suitability of the printing materials for use as a tissue-equivalent phantom material, the HU and SPR of the available printing materials was calculated. First the materials were compared with the conventional HU-SPR conversion from Schneider et al. For tissue-equivalence, the materials used in the phantom should be on the HU-SPR curve. Therefore, we determined the HU and the SPR of PLA, PVA, PET and nylon. We did not include ABS since we did not have the exact composition and were therefore unable to calculate the HU.

The HU were calculated using the photon attenuation at 100 keV taken from the NIST XCOM database [56] combined with formula (1.8). The SPR was calculated using the proton ranges of a 200 MeV proton beam using SRIM [57], which is a program to calculate the range of ions in matter using the Bethe Bloch formula. To simulate the effect of printing with a lower density, the SPR and HU were linearly scaled from 100% to 70% density, as both photon attenuation and proton stopping power scale linearly with the density of the material.

HU measurement of materials

To investigate the suitability of the printing materials for use as tissue-equivalent material using DECT, the sigma-rho method described by Möhler to determine the SPR in the TPS used. To design a phantom that would accurately represent human tissue in a TPS with a DECT using the sigma/rho method, two materials are used in a linear combination to cover part of the sigma-rho space. Therefore these materials must be mixed in such a way that on the length scale of a regular CT-scan (voxel size 1x1x3 mm) this mixture appears homogenously mixed.

To test the possibility of mixing two materials on a small scale, several test prints were made. The aim of these experiments was two-fold: First, to test on what scale the Ultimaker 3 can print two materials together, without making printing errors. Second, to test whether the scale of mixing was small enough to see a homogenous mixing behaviour on a CT scan. The CT-scanner used for these experiments is the SIEMENS SOMATOM Definition Edge.

The printing materials available were PLA with different colours, PLA with bronze-filling, PLA with copper-filling and PLA with carbon fibers. The bronze-filling and copper-filling PLA contain about 35 mass% bronze and copper particles mixed with PLA. The carbon fiber PLA contains 20% carbon fiber mixed with PLA. All materials were bought from ColorFabb BV.

Initially, for these materials the HU was measured by printing a cube of 15 by 15 by 15 millimeter at 100% density, after which these were measured on the CT-scanner at 80 keV and 140 keV, to find two suitable materials for testing the mixing of two materials. To accurately test this, two materials are needed that have a large difference in HU, so they can easily be identified on a CT-scan. After measuring, PLA was used as the low HU material, as PLA is the most common material used in 3D printing, so a lot of expertise is available on using this material. Also it is much cheaper than PLA/carbon fiber. For high HU either copper or brass infused PLA could be used, in this study copper infused PLA was used.

Mixing of two materials using Ultimaker 3

The normal PLA and the copper-filled PLA were printed together to test whether it was possible to make a HU gradient in the CT-scanner. The lay-out of the first print can be seen in Figure 11. We chose to include both a gradient of the amount of copper-filled PLA as well smaller and larger details. This way we could test with one print whether the Ultimaker was able to print small details, and what these small details look like on a CT-image. Initially this model was printed as shown in Figure 11, with the gradient in the x-y plane, while the details in the z-plane are constant. Afterwards, this model was also printed on its side with the gradient in the x-z plane. Because the while PLA was not available, the model was printed using blue PLA.
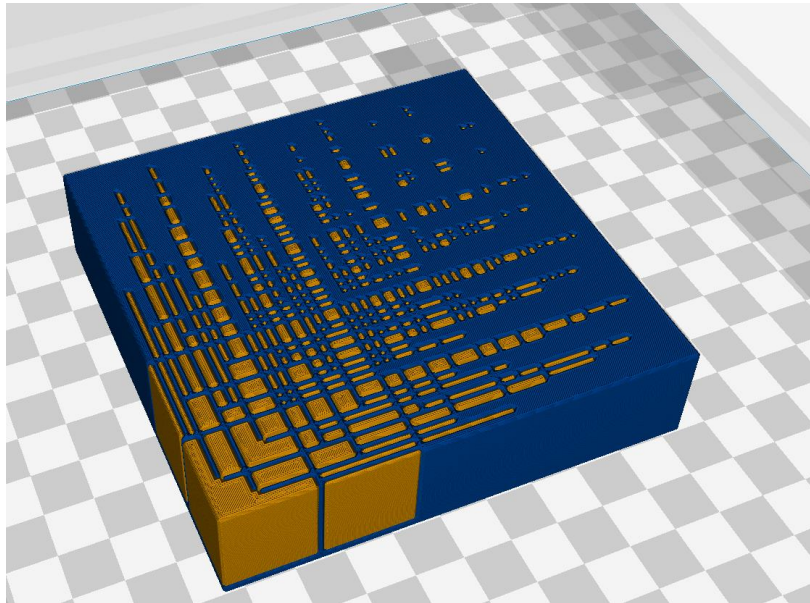

Figure 11. Render of the 3D-printing model used in the experiment. The brown color stands for copper-filled PLA, the blue color represents normal PLA.

The model was made using MATLAB, making a 3-dimensional matrix with zeros corresponding to one material and ones corresponding to the other material. The resolution of this matrix corresponded to the resolution of the print. The Ultimaker 3 was used with a 0.4mm extrusion head, so the minimal width of a plastic printed was 0.4mm. This results in a 0.4mm by 0.4mm resolution in the x-y plane. In the z-direction, the resolution is determined by the height of one layer. For a normal print this is 0.15 mm, but it can be lowered to 0.06mm. As the model was printed using the 'normal' setting, the resolution of the model in MATLAB was 0.4x0.4x0.15mm. Because the model was 40x40x12 mm, the matrix in MATLAB had a size of 100x100x80 numbers.

This matrix was converted to stl-files using the *isosurface* and *stlwrite* function, standard available in MATLAB. This was done for both materials, after which the two models were imported in Cura. Cura was used as a slicer program to convert the stl-files to gcode-files that form the input files for the Ultimaker. For this study MATLAB R2016b and Cura 2.6.2 were used.

The first print attempt, with the details in the x-y plane, failed. The printing head extruded too much plastic, resulting in a pool of molten plastic on top of the print. The over extrusion of the PLA was probably caused by the small details in the printing layer. To test this, another print was made with the details in the x-z plane.

Results

HU-SPR of printing materials

The HU-SPR conversion lines for the selected printing materials are shown in Figure 12. We observed that none of these lines crossed the HU-SPR calibration curve for tissues. This means that none of these materials are suitable as a tissue-equivalent material in a phantom used in a TPS that uses this stoichiometric calibration. Schneider did not provide a parametrization of the calibration curve, therefore the difference in HU and SPR between the printing materials and the calibration curve could not be quantified.
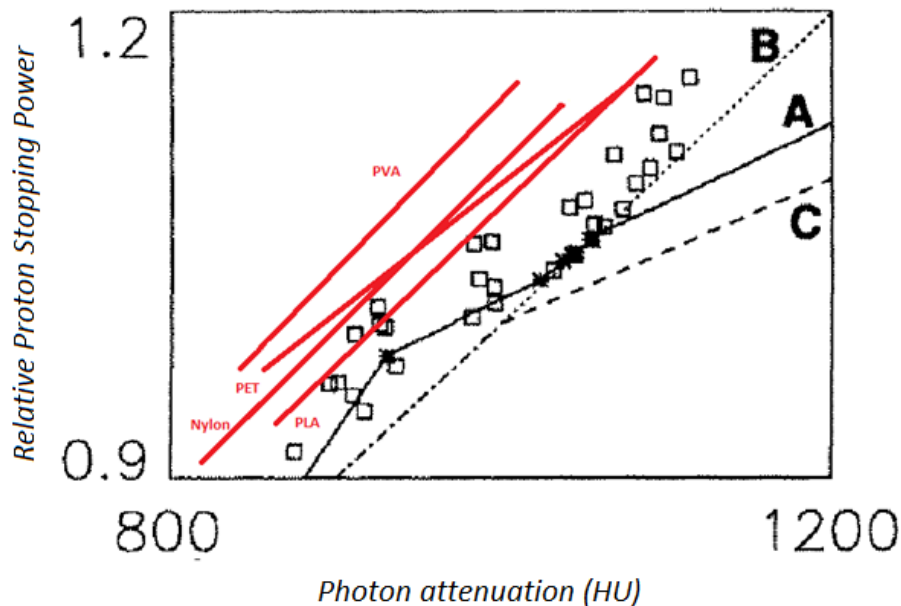

Figure 12. Zoom-in of the HU-SPR calibration curve determined by Schneider et al. [35]**, with the black line the stoichiometric calibration curve as is commonly used nowadays. The crosses represent tissue samples while the squares represent tissue-substitutes. The results of the calculations are shown in red.**

HU determination of printing materials

Results of the measurements of HU of available printing materials are shown in Table 1.

The PLA/copper and PLA/brass had such a high photon attenuation, that the CT-scanner appointed the maximum HU within its scale to these materials. The actual HU is higher, however this is off the scale of the CT-scanner.

Table 1. Measured HU of printing materials available for the Ultimaker 3

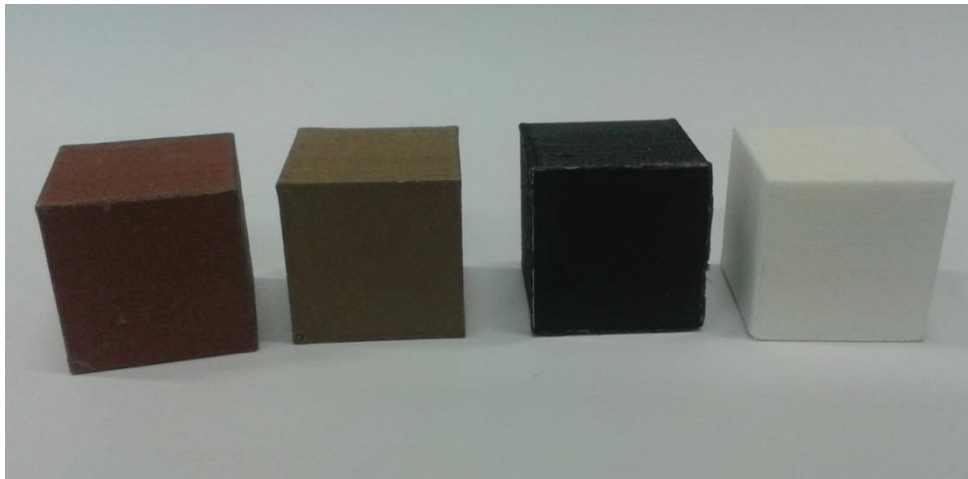| Material	HU
PLA	160 +/- 10
PLA/carbon fiber	175 +/- 25
PLA/copper	3070
PLA/brass	3070

Figure 13. Photograph of the four cubes that were used to determine the HU of the printing materials. From left to right: PLA/Copper, PLA/Brass, PLA/Carbon fiber and white PLA.

Printing of two materials using the Ultimaker 3

The print of the first model to test the capability of the Ultimaker to print two materials on a small scale, are shown in Figure 14 and Figure 15.
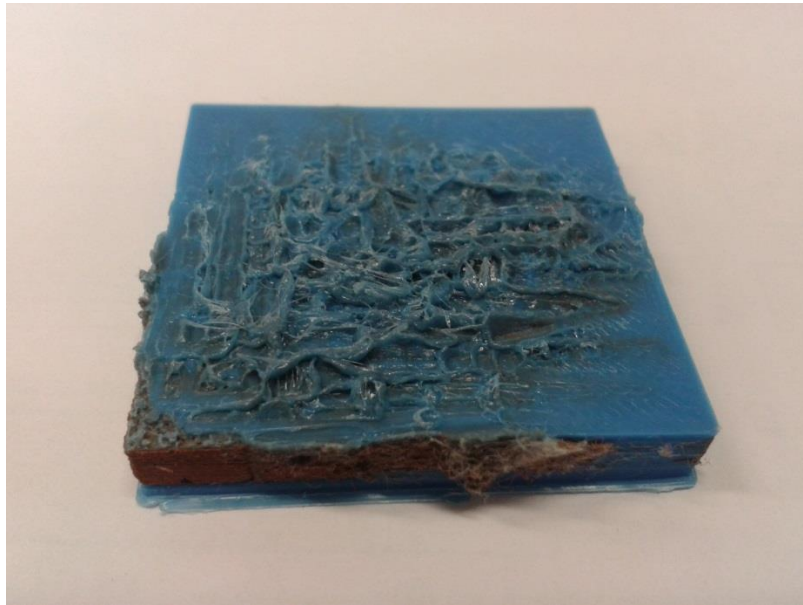

Figure 14. Photograph of the first print attempt of small details with two materials. The print was aborted halfway. The photograph shows the mixing of the two materials on the top of the print, which is the result of too much plastic extruded by the printer
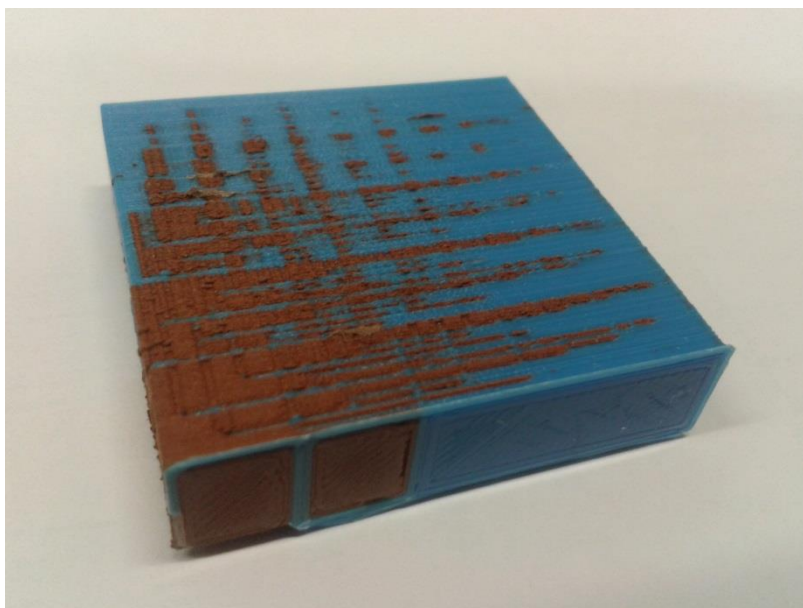
Figure 15. Photograph of the second attempt to print small details. Here the details were printed in the x-z plane instead of the x-y plane. This print looks almost identical to the design (Figure 11).

A CT-scan was made of this model, to compare the HU to the mixture of the two materials. Afterward the CT-slice was compared to the PLA/PLA copper ratio of the model. As the CT-slice thickness was 3 mm, the ratio of PLA/PLA copper was also averaged over 3 mm. Because the CT-values are clipped for high amounts of PLA copper, a fit was made where this effect is corrected.

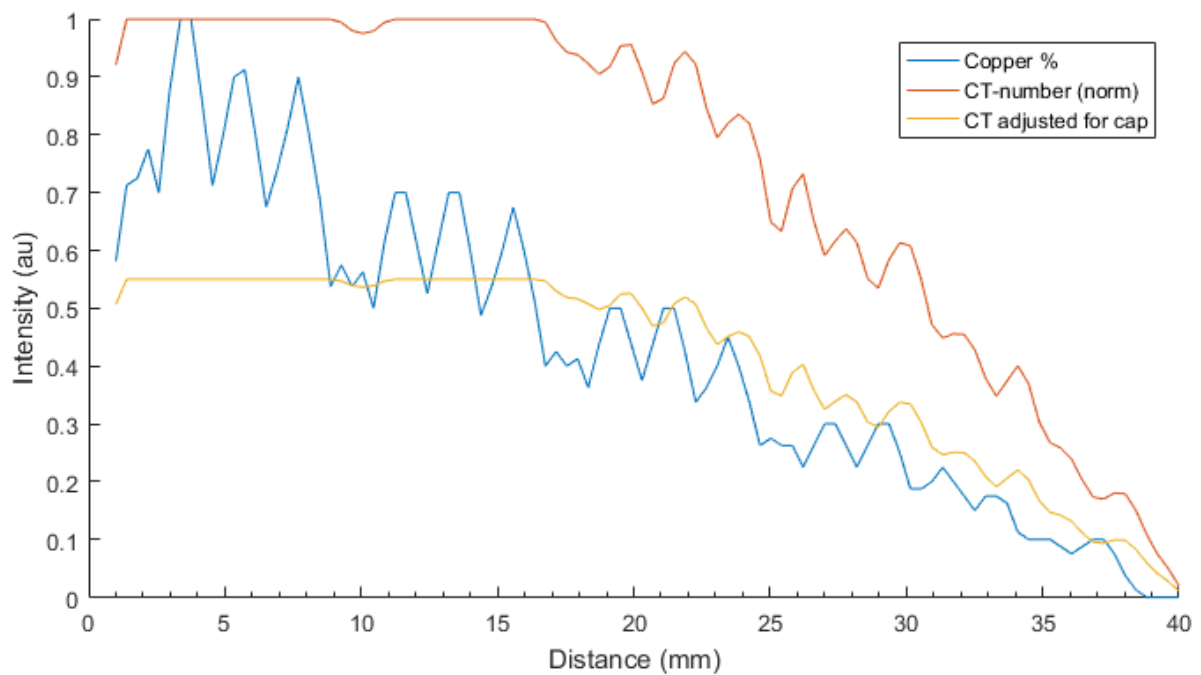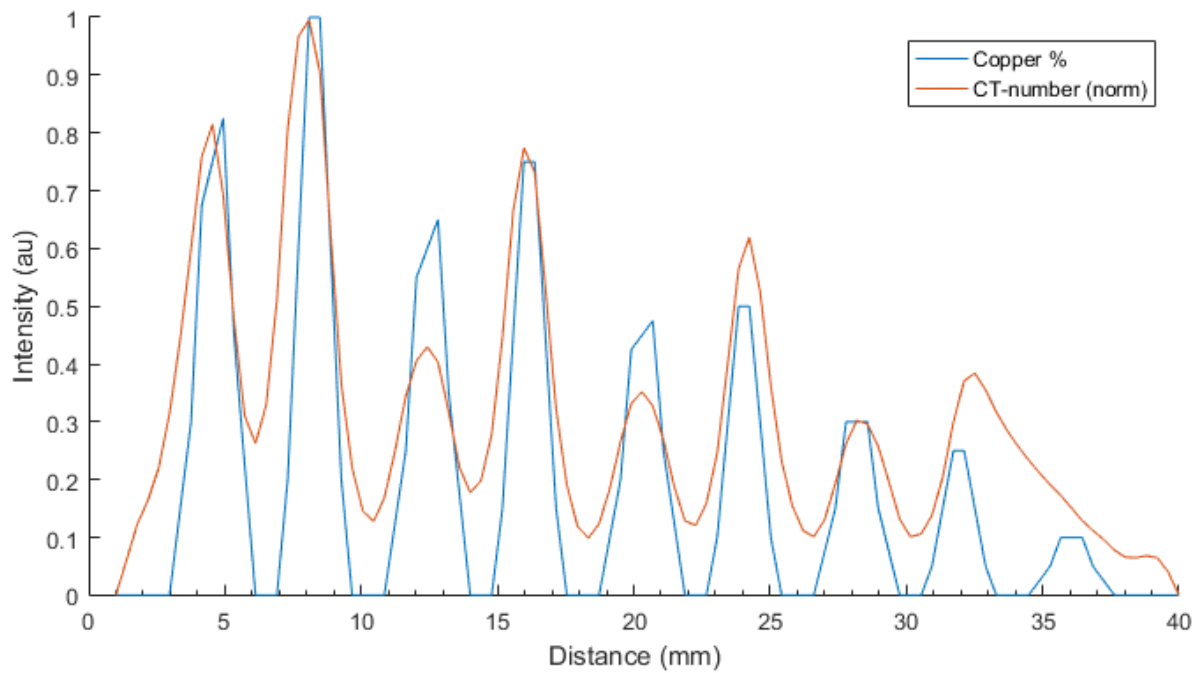**Figure 16. Comparison of the HU of the printed model versus the ratio of PLA and PLA copper filled, as a function of intensity/ratio versus the distance in the x-direction of the model. The top shows this comparison for a cross-section and CT-slice of a low PLA/PLA copper ratio, while the lower graph displays the results for a high PLA/PLA copper ratio. In orange the HU is shown as the ratio of HU divided by the maximum HU of the slice. In blue the ratio of PLA/PLA copper of the slice is shown, which is averaged over the slice thickness of the CT-scan of 3 mm. The ratio was averaged in the x-direction using a moving average function. This is also scaled as ratio divided by the maximum of the ratio. In the lower plot, the HU were scaled to adjust for the capping of the CT numbers when the PLA/PLA copper ratio is very high. This is shown in yellow.**

To do this, the HU were normalized to the ratio of PLA/PLA copper at 20mm distance, as the HU starts declining from there and is thus not clipping anymore. The comparison was done for a high and low ratio of PLA/PLA copper. The results are shown in Figure 16.

These are preliminary results on the correlation between HU and PLA/PLA copper ratio. The location of the CT-slice in the model was estimated by looking at the gradient pattern of the CT-slice and comparing this to the model. The model was assumed to be perfectly aligned to the CT-slice plane.

The top graph indicates that the HU follows peaks in PLA/PLA copper ratio, and it also indicates that the resolution of the CT-scanner appears to be larger than the 1x1x3 mm resolution of the reconstruction used. The large changes in PLA/PLA copper ratio in the top graph on a small length scale are smoothed in the HU curve. The results depicted in the second graph indicate that with a low gradient of PLA/PLA copper, the HU, corrected for the capping, follows the gradient of PLA/PLA copper.

To demonstrate the smoothing of the CT-values with large changes in the PLA/PLA copper ratio, a graph is included that does not have the averaging of the PLA/PLA copper ratio in the x-direction. However, it is still averaged over a slice of 3 mm in the z-direction. This is shown in Figure 17. The changes in PLA/PLA copper are very abrupt and within one or two millimeter. The CT-values however takes up to 3 mm to change, for example from 1mm to 4 mm. This shows that although the voxel size is small, the inaccuracy of the CT-scanner to detect such large changes in photon attenuation in a short distance is larger. This is promising for our new technique, as the level of detail required for the mixing is in the order of millimeters instead of hundreds of micrometers.

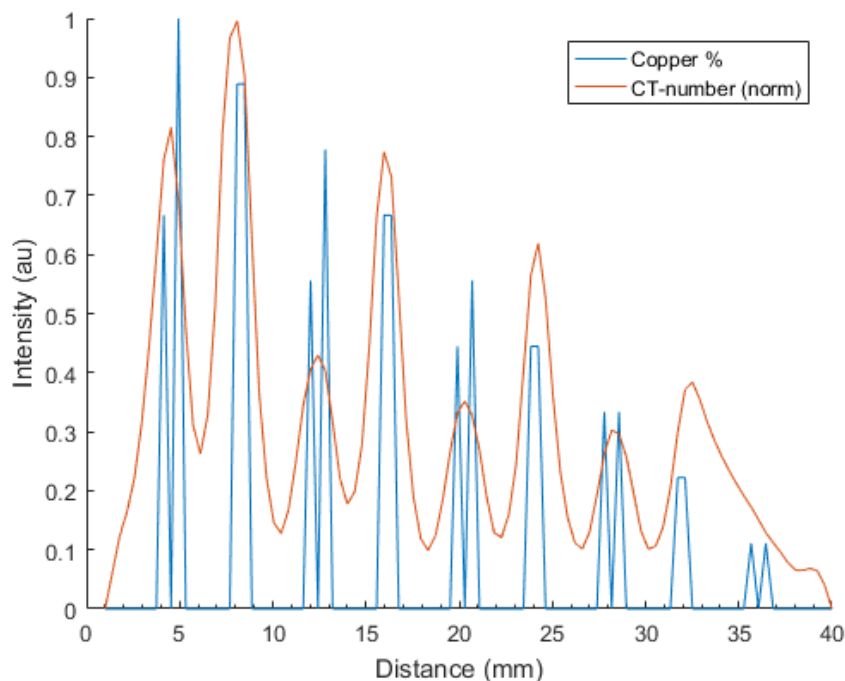**Figure 17. This graph shows the same data as the top graph of Figure 16, but without a moving average in the x-direction. This shows that the CT-values are smoothed in the x-direction. In blue the ratio of PLA/PLA copper of the slice is shown, which is averaged over the slice thickness of the CT-scan of 3 mm. In orange the HU is shown as the ratio of HU divided by the maximum HU of the slice.**

Discussion

The results indicate that mixing of materials using a 3D-printer on a level that would seem homogeneous is feasible. Unfortunately, there are also some difficulties that we ran into during this research, which will be elaborated in this chapter.

Printing materials

The first experiment showed that the diversity of materials available for 3D-printing is very limited. When looking for tissue-substitute materials, most of the plastics available can be used as an substitute for soft tissue, although not ideal. For bone tissue, a suitable substitute is not yet available. The only materials that are commercially available with a higher effective Z consist of PLA mixed with metals such as copper or brass. The photon attenuation and effective Z of these materials is much higher than that of bone.

The results of the first experiment show that none of the commercially available materials are as close as other tissue-substitute materials to the stoichiometric calibration curve published by Schneider et al., the calibration that is used in the majority of TPSs. This makes it impossible to print a tissue-equivalent phantom that can be used in the short-term using these materials. In the long run, we expect DECT to be implemented further in the clinical practise, which will speed up implementation of calibrations based on DECT such as proposed by Hünemohr and Möhler. As discussed in the theory, this would enable the use of two well-chosen materials to mix these with different ratios in order to represent human tissues in the (σ, L) space.

This demands new printing materials, which can be made by mixing a new plastic and using this for printing. Machines are commercially available to make printing filaments from plastic pellets for a few thousand euros. Also PLA is commercially available as pellets. This can be used to make a new printing material based on PLA, infused with for example calciumoxide. When mixed with the right mixing ratio, this could come very close to human bone tissue, which also consists of hydrogen, carbon, oxygen and calcium atoms. The advantage of using PLA as a base is that the printing properties remain almost the same, making it automatically compatible with the current 3D-printers. When the results of using such a material are promising, this could be used as a start to design a whole new material for both soft and bone tissue, which would lie on the tissue line in the sigma/rho space.

A more short-term application, with potentially high gain, would be to use plastics currently used as tissue-substitutes such as PMMA, and turn these into printing filaments. This way a phantom can be printed that is tissue-equivalent for photons, and as tissue-equivalent for protons as commercially available phantoms currently are. Although not perfectly tissue-equivalent for protons, small geometric details can be added that cannot be added with current casting techniques.

It might also be interesting to investigate the tissue-substitute materials close to the stoichiometric calibration line. If these materials are plastics with a melting point in the range that the 3D-printer can be heated (roughly between 100 and 250 degrees Celsius), these could also be turned into printing filaments and used for fabrication of phantoms that can be used in the current clinical practise. Combined with the possibility of 3D-printing to include small geometric changes that are

significant for proton treatment planning, such as small air cavities and small high-Z fragments, this could be an interesting application. This would require the investment in a filament maker.

3D-printing problems

The photograph of the failed print in Figure 14 illustrates the potential difficulties with 3D-printing. We encountered problems that according to the specifications should not happen. The resolution of the printer in the z-axis is very high and independent of changes in material. In the x-y-plane this is different. The printing head lays down a line of plastic, which is melted in the extruder. The amount of plastic that is being ejected is controlled with a motor that pushes the filament through the extruder. Under normal conditions the flow of plastic is constant while the head moves. When changing material or when there is an area where no printing should occur, the filament is retracted using the motor and the flow stops. This mechanism is not very accurate, so a small amount of plastic can leak during retraction. This results in overextrusion of your printing material, as shown in Figure 14. Normally this is not a problem as this retraction only occurs once every few minutes and the leakage is very small compared to the amount of plastic printed. In our case however, a print was made with a dot-like pattern of the material, as shown in Figure 11. Now the filament is retracted each time the printing head goes from one dot to the other, so the leakage to print ratio becomes much larger, resulting in a failed print.
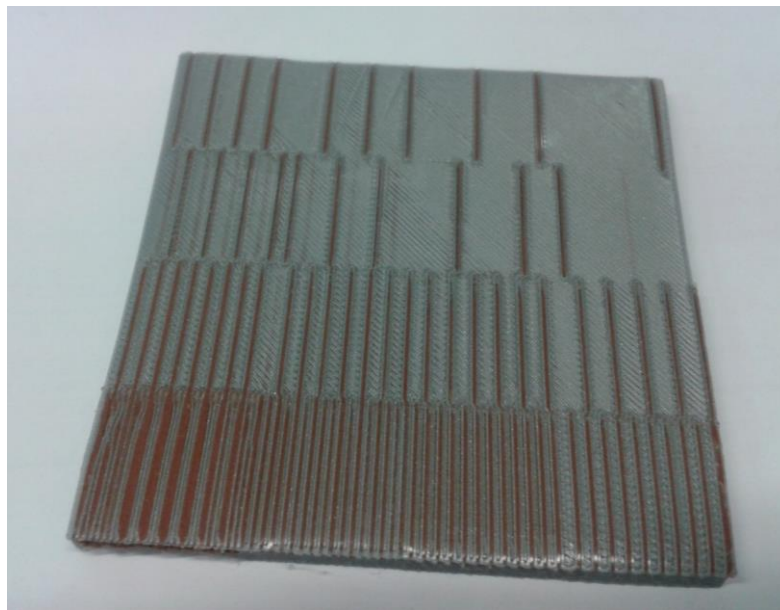

Figure 18. Photograph of the last model, which failed printing. The model consists of 16 squares of 1x1 millimeter with a constant ratio between PLA and PLA copper filled. This was done by adjusting the ratio between printed lines of PLA and PLA copper.

The second print shows that this can be solved by not printing dots. The orientation of the model was changed so that the printing layers now consisted of lines in the y-direction. Because less retraction was needed, the leakage to print ratio was lowered and the print succeeded. In the future, the printing models should be designed in such a way that dots are avoided. A resolution of 400 µm in the width of the plastic line printed can still be achieved, but the length of the line should be a few millimetre at least. This decreases the resolution that can be achieved using 3D-printing. The results however indicate that this might not be a problem as the resolution of the CT-scanner is also quite large.

When trying to print our last model, we encountered a new problem. A photograph of the printed model in included in Figure 18. Because of the difficulties encountered with the previous model, this model consisted of lines of PLA and PLA copper, where the ratio between the two materials was adjusted by adjusting the line density of both. This way the problem of overextrusion was prevented, however a new problem arose: after a few hours of printing the PLA copper stopped printing. It turned out that the copper filament was broken at the motor area that pushes and pulls the filament to and from the extruder. Every time the filament is retracted, the wheel of the motor damages the filament due to the friction. Because the PLA copper filament is very brittle compared to normal PLA, the high amount of retractions resulted in breaking of the filament. One way of preventing this is to decrease the amount of retractions even further, for example by connecting the individual lines by another line of PLA copper in the model, so that the filament is not retracted when going from one line to the other. Unfortunately, this does increase the PLA copper to PLA ratio, so this has to be accounted for when the model is made. Another possibility would be to print a large area of PLA copper next to the model. This way a lot of PLA copper is printed, thus the filament moves further through the machine. This way the part of the filament that is in the motor area is changed every layer, and the damage to the filament is spread more, preventing it from breaking. This should be tested with further research.

A last short-coming of the 3D-printer has to be mentioned: when printing at 100% density, printing time increases tremendously when the size of the print increases. We have tried printing a 4x4x1 cm solid rectangular shape on the highest details setting, which would have taken about 48 hours to print, which is 3 hours per cubic centimeter. Assuming this scales linearly, with a head-shaped real-size phantom having a volume of about 5 liters, it would take 15.000 hour to print one head-phantom, or 625 days. When using slightly lower resolution settings (100 μm z-direction resolution instead of 20 μm), the time to print goes down with a factor 5 to 10, depending on the complexity of the geometry.

This is a limitation that cannot be solved at the moment. As mentioned before, 3D-printing is a relatively new concept that is still rapidly developing. It could be that printing times will reduce in the coming decade due to new developments. Also, the printer used in this study is a consumer type, not an industrial one. Chances are that industrial printers will be faster. Another way to counter this problem is by printing multiple parts in parallel, after which the part can be assembled together to from one phantom.

Other recommendations

It might be interesting to widen the scope of the research. During this study, the focus has been on the possibility to ultimately design an anthropomorphic phantom for proton therapy. However, it might be interesting to use 3D-printing for the manufacturing of non-anthropomorphic phantoms. This has already been done for photons [58], but can also be done for protons. For example, a phantom made of PLA with small air gaps can be easily designed and printed, and would be an interesting test for the TPS.

The radiation interaction properties of currently available printing materials are not yet published, and could also be studied as part of this research. The literature in the field of phantoms and 3D-

printing [9], [59]–[62], lacks research done on making new materials for tissue-equivalence. Most studies reported that the materials are not tissue-equivalent, but only few address this as a problem for the design of a phantom. Also Leary pointed out that not much information is published on the currently commercially available printing materials, and, quoting, *"A significant opportunity exists in experimentally obtaining this information (*the radiographic properties*) through testing and experimentation."* [62] Especially when research is continued into the design of new printing materials that are tissue-equivalent, it would be valuable to be able to compare these materials with the commercially available ones, in terms of radiation interaction properties.

A more novel research is to look into the slicer software used to convert a stl-model into gcode, which is the input for the 3D-printer. The slicer determines how the lines of plastic are laid down and how the printing head moves. The current slicer software available is not optimized for the type of models we use. During printing, it was observed that the printing head sometimes moves for more than 5 seconds without printing, before it prints a single line, and then starts moving without printing again. This increases the printing time a lot. Because current software is based on models that are printed hollow, it is suspected the algorithm is not suitable for handling the type of prints done in this study. There are a few well-known and developed slicer software that are open source, such as Slic3r, that could give insight into these problems. Although commercially maintained by Ultimaker, Cura is also open-source. Maybe it is possible to optimize the code of these slicers for high density prints with small, dual material details.

Lastly it might be profitable to look into the possibilities of industrial grade 3D-printers. These are more advanced and might give more possibilities and solutions to our current problems. It might be wise to co-operate with the 3D-printing industry at some point. At the moment, the expertise of 3D-printing is spread across multiple departments and DEMO, and there is no overview of all the knowledge that is available in-campus. If all this knowledge would be combined, and a platform would be created to co-operate with the industry, I think a lot of time and effort can be spared.

Conclusion

Current phantoms are not suited for QA in proton therapy, as they are not tissue-equivalent for both photons and protons and lack the level of detail in human anatomy required for accurate QA. 3D-printing offers the possibility to print phantoms that include small geometric detail such as air gaps and density gradients.

The stoichiometric calibration curve for HU-SPR conversion currently used in most TPS does not provide possibilities to make a tissue-equivalent phantom using currently available materials. A new HU-SPR conversion using DECT and the rho-sigma method determines the SPR directly using the electron density and the mean ionization potential of the materials. With this method it is possible to ideally use two materials in a linear combination to build a tissue-equivalent material which can represent the complete human tissue range. This requires the mixing of these materials on such a small scale that these appear homogeneously mixed in a CT-image.

These preliminary experiments indicate that it is possible to mix two materials on such a small scale that it appears homogeneously mixed on the CT-image. However additional research is needed to further investigate the possibilities in 3D-printing two materials on such a small scale.

The continuation of this research should be focused on two research topics. First the printing materials: The exact radiation properties of currently available printing materials are yet unknown. The possibilities of using available tissue-substitute materials as printing materials to print phantoms could be investigated. Especially the last design of new materials that cover the sigma, L space of human tissue is needed to enable the 3D-printing of a truly tissue-equivalent phantom for proton therapy.

Second the technique of 3D-printing should be further investigated. The limitations in printing two materials together on a small scale should be studied. The printing of small amounts of one material into the other material can be optimized further. An algorithm should be found for mixing two materials, dots, lines or other geometries automatically. These problems might partially be solved when other, industrial printers are used or when other materials are used. As 3D-printing is a novel technique, future development might take away some of the encountered problems.

References

[1]   R. R. Wilson, "Radiological use of fast protons," *Radiology*, vol. 47, no. 5, pp. 487–491, 1946.

[2]   J. M. Slater, J. O. Archambeau, D. W. Miller, M. I. Notarus, W. Preston, and J. D. Slater, "The proton treatment center at Loma Linda University Medical Center: rationale for and description of its development," *Int. J. Radiat. Oncol. Biol. Phys.*, vol. 22, no. 2, pp. 383–389, 1992.

[3]   H. Paganetti, "Proton Therapy: History and Rationale," *Prot. Ther. Phys.*, pp. 1–18, 2016.

[4]   H. Paganetti, *Proton therapy physics*. CRC Press, 2016.

[5]   "Proton Cancer Treatment." [Online]. Available: http://www.proton-cancer-treatment.com/proton-therapy/principles-of-proton-therapy/. [Accessed: 28-Aug-2017].

[6]   A. W. Chan and N. J. Liebsch, "Proton radiation therapy for head and neck cancer," *J. Surg. Oncol.*, vol. 97, no. 8, pp. 697–700, 2008.

[7]   J. Wu, N. Aage, R. Westermann, and O. Sigmund, "Infill Optimization for Additive Manufacturing--Approaching Bone-like Porous Structures," *IEEE Trans. Vis. Comput. Graph.*, 2017.

[8]   D. R. White, "The design and manufacture of anthropomorphic phantoms," *Radiat. Prot. Dosimetry*, vol. 49, no. 1–3, pp. 359–369, 1993.

[9]   J. I. Gear, C. Long, D. Rushforth, S. J. Chittenden, C. Cummings, and G. D. Flux, "Development of patient-specific molecular imaging phantoms using a 3D printer Development of patient-specific molecular imaging phantoms using a 3D printer," *Med. Phys.*, vol. 82502, no. 41, pp. 2012–2015, 2014.

[10]   R. Kienbock, "On the Quantimetric Method," *Arch. Roentgen Ray*, vol. 11, no. 1, pp. 17–20, 1906.

[11]   T. Christen, "Messung und Dosierung der Röntgenstrahlen," *Fortschritte auf dem Gebiete der Roentgenstrahlen. Ergaenzungsband*, 1913.

[12]   L. Baumeister, "Roentgen-Ray Measurements," *Acta radiol.*, no. 4–5, pp. 418–429, 1923.

[13]   W. V Mayneord, "Notes on Three Problems of Gamma Ray Therapy," *Br. J. Radiol.*, vol. 6, no. 70, pp. 598–614, 1933.

[14]   L. A. DeWerd and M. Kissick, *The Phantoms of Medical and Health Physics*. 2014.

[15]   A. Westman, "A Simplified Dosimetric Method in Gynecological Deep Roentgentherapy TT -," *Acta Radiol. TA -*, vol. Original S, no. 1, pp. 68–75, 1924.

[16]   A. Wambersie and D. R. White, "ICRU activity in the field of phantoms in diagnostic radiology," *Radiat. Proection Dosim.*, vol. 43, no. 1/4, pp. t1--t14, 1992.

[17]   D. R. White, "Tissue substitutes in experimental radiation physics.," *Med. Phys.*, vol. 5, no. 6, pp. 467–479, 1978.

[18]   D. R. White, "The specifications of 25 phantoms presented at the Wurburg Workshop (June, 1992)," *Radiat. Prot. Dosimetry*, vol. 49, no. 1–3, pp. 371–386, 1993.

[19]   M. Stovall, P. Balter, W. F. Hanson, and A. Cole, "Quality audit of radiosurgery dosimetry using mailed phantoms," *Med. Physics1*, vol. 22, p. 1009, 1995.

[20]   A. Molineu *et al.*, "Design and implementation of an anthropomorphic quality assurance phantom for intensity-modulated radiation therapy for the Radiation Therapy Oncology Group," *Int. J. Radiat. Oncol. Biol. Phys.*, vol. 63, no. 2, pp. 577–583, 2005.

[21]   D. F. Caruthers, G. S. Ibbott, and D. S. Followill, "Commissioning an Anthropomorphic Spine and Lung Phantom for Remote Dose Verification of Institutions Participating in RTOG 0631," *Med. Phys.*, vol. 36, p. 2651, 2009.

[22]   CIRS, "Proton Therapy Dosimetry Head Model 731-HN - Data Sheet," 2017. [Online]. Available: http://www.cirsinc.com/file/Products/731-HN/731HN DS 042716.pdf. [Accessed: 14-Aug-2017].

[23]   P. Farace, R. Righetto, and A. Meijers, "Pencil beam proton radiography using a multilayer ionization chamber," *Phys. Med. Biol.*, vol. 61, no. 11, p. 4078, 2016.

[24]   Z. Li, R. Slopsema, S. Flampouri, and D. Yeung, "Quality Assurance and Commissioning," *Prot. Ther. Physics. Ser. Ser. Med. Phys. Biomed. Eng. ISBN 978-1-4398-3644-6. CRC Press. Ed. by Harald Paganetti, pp. 221-264*, pp. 221–264, 2011.

[25]   R. E. Alvarez and A. Macovski, "Energy-selective reconstructions in x-ray computerised tomography," *Phys. Med. Biol.*, vol. 21, no. 5, p. 733, 1976.

[26]   N. Hünemohr, B. Krauss, C. Tremmel, B. Ackermann, O. Jäkel, and S. Greilich, "Experimental verification of ion stopping power prediction from dual energy CT data in tissue surrogates," *Phys. Med. Biol.*, vol. 59, no. 1, p. 83, 2013.

[27]   S. M. Seltzer, "An assessment of the role of charged secondaries from nonelastic nuclear interactions by therapy proton beams in water," *NIST Interagency/Internal Rep. (NISTIR)-*, 1993.

[28]   H. Paganetti and M. Goitein, "Radiobiological significance of beamline dependent proton energy distributions in a spread-out Bragg peak," *Med. Phys.*, vol. 27, no. 5, pp. 1119–1126, 2000.

[29]   H. Paganetti and M. Goitein, "Biophysical modelling of proton radiation effects based on amorphous track models," *Int. J. Radiat. Biol.*, vol. 77, no. 9, pp. 911–928, 2001.

[30]   G. Moliere, "Theorie der streuung schneller geladener teilchen i. einzelstreuung am abgeschirmten coulomb-feld," *Zeitschrift für Naturforsch. A*, vol. 2, no. 3, pp. 133–145, 1947.

[31]   G. Moliere, "Theorie der streuung schneller geladener teilchen ii mehrfach-und vielfachstreuung," *Zeitschrift für Naturforsch. A*, vol. 3, no. 2, pp. 78–97, 1948.

[32]   J. Deasy, "ICRU Report 49, stopping powers and ranges for protons and alph particles," *Med. Phys.*, vol. 21, no. 5, pp. 709–710, 1994.

[33]   B. Gottschalk, "Physics of proton interactions in matter," *Prot. Ther. Phys.*, pp. 19–60, 2011.

[34]   H. Bethe and W. Heitler, "On the stopping of fast particles and on the creation of positive electrons," in *Proceedings of the Royal Society of London A: Mathematical, Physical and Engineering Sciences*, 1934, vol. 146, no. 856, pp. 83–112.

[35]   U. Schneider, E. Pedroni, and A. Lomax, "The calibration of CT Hounsfield units for

radiotherapy treatment planning.," *Phys. Med. Biol.*, vol. 41, no. 1, pp. 111–24, 1996.

[36] B. Schaffner and E. Pedroni, "The precision of proton range calculations in proton radiotherapy treatment planning: experimental verification of the relation between CT-HU and proton stopping power," *Phys. Med. Biol.*, vol. 43, no. 6, p. 1579, 1998.

[37] P. Andreo, "On the clinical spatial resolution achievable with protons and heavier charged particle radiotherapy beams," *Phys. Med. Biol.*, vol. 54, no. 11, p. N205, 2009.

[38] H. Paganetti, "Range uncertainties in proton therapy and the role of Monte Carlo simulations," *Phys. Med. Biol.*, vol. 57, no. 11, p. R99, 2012.

[39] W. D. Newhauser, A. Giebeler, K. M. Langen, D. Mirkovic, and R. Mohan, "Can megavoltage computed tomography reduce proton range uncertainties in treatment plans for patients with large metal implants?," *Phys. Med. Biol.*, vol. 53, no. 9, p. 2327, 2008.

[40] O. Jäkel and P. Reiss, "The influence of metal artefacts on the range of ion beams," *Phys. Med. Biol.*, vol. 52, no. 3, p. 635, 2007.

[41] R. L. Grant *et al.*, "Relative stopping power measurements to aid in the design of anthropomorphic phantoms for proton radiotherapy," *J. Appl. Clin. Med. Phys.*, vol. 15, no. 2, pp. 121–126, 2014.

[42] R. W. Schulte *et al.*, "Density resolution of proton computed tomography," *Med. Phys.*, vol. 32, no. 4, pp. 1035–1046, 2005.

[43] H. Muraishi *et al.*, "Evaluation of spatial resolution for heavy ion CT system based on the measurement of residual range distribution with HIMAC," *IEEE Trans. Nucl. Sci.*, vol. 56, no. 5, pp. 2714–2721, 2009.

[44] J. Telsemeyer, O. Jäkel, and M. Martišíková, "Quantitative carbon ion beam radiography and tomography with a flat-panel detector," *Phys. Med. Biol.*, vol. 57, no. 23, p. 7957, 2012.

[45] I. Rinaldi *et al.*, "Experimental characterization of a prototype detector system for carbon ion radiography and tomography," *Phys. Med. Biol.*, vol. 58, no. 3, p. 413, 2013.

[46] T. G. Flohr *et al.*, "First performance evaluation of a dual-source CT (DSCT) system," *Eur. Radiol.*, vol. 16, no. 2, pp. 256–268, 2006.

[47] R. A. Rutherford, B. R. Pullan, and I. Isherwood, "Measurement of effective atomic number and electron density using an EMI scanner," *Neuroradiology*, vol. 11, no. 1, pp. 15–21, 1976.

[48] T. R. C. Johnson *et al.*, "Material differentiation by dual energy CT: initial experience," *Eur. Radiol.*, vol. 17, no. 6, pp. 1510–1517, 2007.

[49] M. Bazalova, J.-F. Carrier, L. Beaulieu, and F. Verhaegen, "Dual-energy CT-based material extraction for tissue segmentation in Monte Carlo dose calculations," *Phys. Med. Biol.*, vol. 53, no. 9, p. 2439, 2008.

[50] G. Landry *et al.*, "Extracting atomic numbers and electron densities from a dual source dual energy CT scanner: experiments and a simulation model," *Radiother. Oncol.*, vol. 100, no. 3, pp. 375–379, 2011.

[51] M. Yang, G. Virshup, J. Clayton, X. R. Zhu, R. Mohan, and L. Dong, "Dual-energy CT imaging for measuring proton stopping ratios," *Phys. Med. Biol.*, vol. 55, pp. 1343–1362, 2010.

[52]   C. Möhler, P. Wohlfahrt, C. Richter, and S. Greilich, "Range prediction for tissue mixtures based on dual-energy CT," *Phys. Med. Biol.*, vol. 61, no. 11, p. N268, 2016.

[53]   S. M. Seltzer and M. J. Berger, "Evaluation of the collision stopping power of elements and compounds for electrons and positrons," *Int. J. Appl. Radiat. Isot.*, vol. 33, no. 11, pp. 1189–1218, 1982.

[54]   W. H. Bragg and R. Kleeman, "XXXIX. On the α particles of radium, and their loss of range in passing through various atoms and molecules," *London, Edinburgh, Dublin Philos. Mag. J. Sci.*, vol. 10, no. 57, pp. 318–340, 1905.

[55]   R. Scopigno, P. Cignoni, N. Pietroni, M. Callieri, and M. Dellepiane, "Digital Fabrication Techniques for Cultural Heritage: A Survey," in *Computer Graphics Forum*, 2017, vol. 36, no. 1, pp. 6–21.

[56]   M. J. Berger, J. H. Hubbell, S. M. Seltzer, J. Chang, J. S. Coursey, and R. Sukumar, "XCOM: photon cross sections database. NBSIR 87–3597. 1998." .

[57]   J. F. Ziegler, M. D. Ziegler, and J. P. Biersack, *SRIM: the stopping and range of ions in matter*. Cadence Design Systems, 2008.

[58]   M. F. Bieniosek, B. J. Lee, and C. S. Levin, "3D printing for cost-effective, customized, reusable multi-modality imaging phantoms," in *Nuclear Science Symposium and Medical Imaging Conference (NSS/MIC), 2013 IEEE*, 2013, pp. 1–3.

[59]   E. D. Ehler, B. M. Barney, P. D. Higgins, and K. E. Dusenbery, "Patient specific 3D printed phantom for IMRT quality assurance.," *Phys. Med. Biol.*, vol. 59, no. 19, pp. 5763–5773, 2014.

[60]   R. Mayer, P. Liacouras, A. Thomas, M. Kang, L. Lin, and C. B. Simone, "3D printer generated thorax phantom with mobile tumor for radiation dosimetry," *Rev. Sci. Instrum.*, vol. 86, no. 7, 2015.

[61]   J. I. Gear *et al.*, "Abdo-Man: a 3D-printed anthropomorphic phantom for validating quantitative SIRT.," *EJNMMI Phys.*, vol. 3, no. 1, p. 17, 2016.

[62]   M. Leary *et al.*, "Additive manufacture of custom radiation dosimetry phantoms: An automated method compatible with commercial polymer 3D printers," *Mater. Des.*, vol. 86, pp. 487–499, 2015.